Toward Voxel Level Control for Laser Powder Bed Fusion Additive Manufacturing Processes

Ho Yeung, Jorge Neira
National Institute of Standards and Technology, Gaithersburg, MD 20899

Abstract

In the Laser Powder Bed Fusion (LPBF) additive manufacturing (AM) process, a high-speed scanning laser beam is employed to construct components by melting and fusing metal powder together. While AM is generally characterized as a layer-by-layer technique, LPBF builds can also be conceptualized on a voxel-by-voxel basis, utilizing a point laser heating source. As a result, managing the LPBF process at the voxel level – that is, focusing on individual 3D printing elements or volume pixels – will be highly beneficial. In this study, we will explore the laser control requirements necessary for achieving voxel-level precision in the LPBF process and demonstrate these concepts through experiments.

Introduction

Laser Powder Bed Fusion (LPBF) is an advanced additive manufacturing (AM) technique that employs a high-energy laser beam, guided by a pair of mirrors driven by galvanometer motors (galvo), to selectively melt metallic powder and construct a part layer by layer [1,2]. This process allows for the direct fabrication of parts from three-dimensional (3D) computer-aided designs. LPBF excels at creating complex geometries that are challenging or even impossible to manufacture using conventional methods. LPBF utilizes one or more moving point heat sources, and the process can be conceptually discretized into minute volumes—namely, voxels—which proceed to accumulate as material is consolidated. This study aims to discuss strategies for achieving voxel-level control in LPBF, fully unlocking its potential capabilities.

The term "voxel-level control" refers to the ability to control each and every voxel in a 3D build. In the context of metal AM, this control can be fine-tuned to achieve desired material properties such as microstructure, phase, and surface roughness at specific locations. Despite the potential benefits, a literature survey reveals limited discussion specifically focusing on voxel-level control in metal LPBF processes. This lack of focus is unsurprising, given that most current LPBF machines still rely on "line-wise" control technology, which is inherently unsuited for voxel-level manipulation.

In the LPBF process, the 3D part model is initially sliced into two-dimensional (2D) layers, which are then filled with one-dimensional (1D) scan paths, as depicted in Figure 1. In current LPBF machinery, the vast majority of1D scan paths consist of only straight lines, which are then directly sent to a 'black box' machine controller for execution. Consequently, the 1D scan path level represents the lowest level at which users can exert control. This is referred to as line-wise control. Such line-wise control restricts users to applying constant laser power and scan speed to each line, and typically many adjacent lines (i.e., ‘hatches’), so that a specified area is filled with lines that utilize these same, fixed laser parameters. However, the LPBF process is

highly sensitive to local thermal conditions, and defects may develop if the build process is not adapted to the continuous changes in these conditions [3,4].

To address this challenge, we have developed pointwise control for the LPBF process and integrated it into the National Institute of Standards and Technology's (NIST) Additive Manufacturing Metrology Testbed (AMMT) [5]. As illustrated in Figure 1, an interpreter layer was added into the simple AM (SAM) utility software [6]. This layer transforms the 1D lines into zero-dimensional (0D) points, represented by their (x, y) coordinates, by applying a motion control profile and a 10 µs sampling interval. The laser power and diameter, as well as the triggers for the monitoring devices, are assigned to each point to create the time-stepped digital commands [6]. These commands are executed via a custom-built controller (Figure 1), and the updated information are relayed to various hardware modules at 10 µs intervals. This is equivalent to 10 µm distance at a nominal scan speed of 1 m/s, rendering the laser control effectively continuous through this pointwise control.

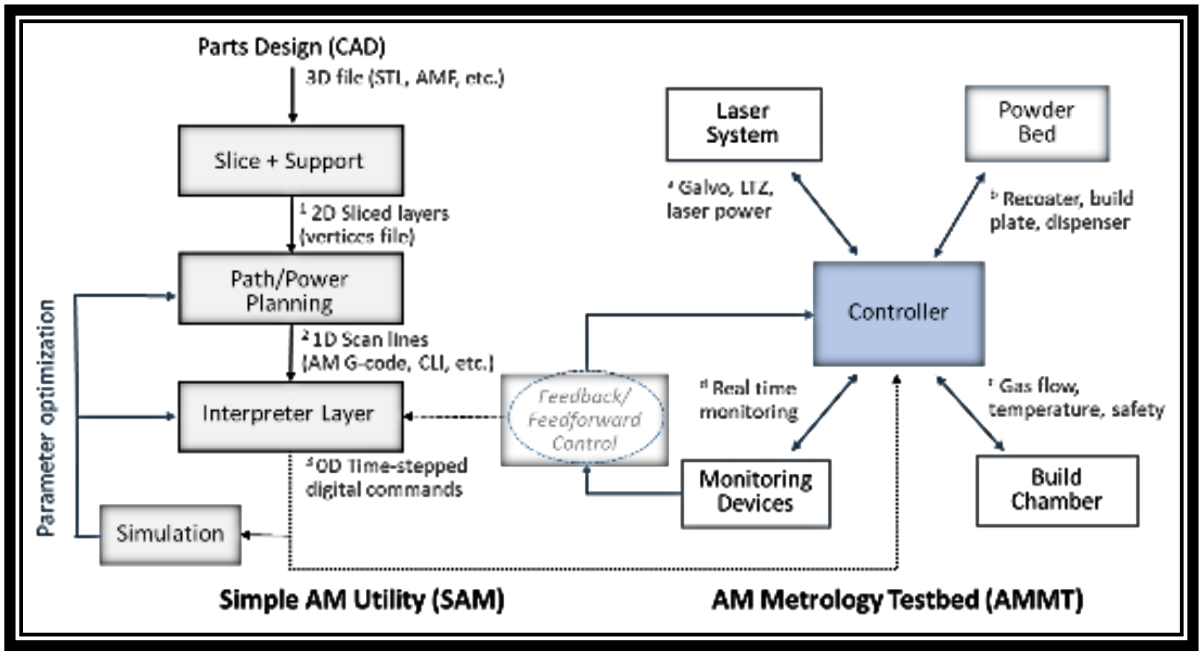

Figure 1. LPBF pointwise control framework

Our discussion on voxel-level control will be based on pointwise laser control. However, it is important to distinguish between these two types of control. Pointwise control refers to the system's ability to vary laser scan parameters at fine time intervals, while voxel-level control assigns laser parameters for each point within each voxel to achieve location-dependent desired material properties or qualities. The link between a moving point-heat source and influence on spatially or voxel-defined material qualities is established via control of the temperature field. Given that the properties of AM parts are strongly influenced by the local temperature field, pointwise control becomes a vital tool for effectively managing this field.

Temperature field control scan strategies

Two types of temperature field control scan strategies were developed and compared with conventional line scans. The first type involves elliptical scan strategies, as depicted in Figure 2. The elliptical scan strategy is defined by the major and minor axes of the ellipse, labeled as ‘a’ and ‘b’; and the hatching distance, represented as ‘h’ in the figure. This elliptical movement has been incorporated into the SAM AM G-code interpreter [6], allowing for the elliptical path shown in the figure to be programmed using a single AM G-code line—such as *G66 X2.2 Y0 A0.5 B0.25 H0.1*.

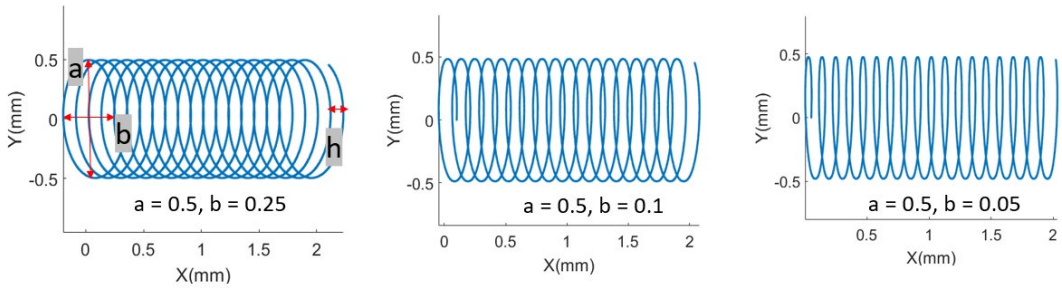

Figure 2. Sample elliptical scan strategies. The terms 'a' and 'b' represent the major and minor axes of the ellipse, respectively, while 'h' denotes the maximum shifting of the ellipse along its minor axis.

The adoption of an elliptical scan strategy was influenced by the author's previous study, which compared the hardness of stainless steel 17-4 parts constructed using various scan methods. That study observed a significant improvement in part hardness when employing an elliptical scan strategy with specific parameters [7]. These strategies have been revisited in the current study, which utilizes an ultra-fast galvo system capable of achieving an acceleration of 5×10^7 mm/s^2, and a high-sensitivity in-situ melt pool (MP) monitoring camera capable of capturing MP boundaries at 25 µs integration times.

It should be noted that the term ‘spiral’ was initially used to describe the scan strategy in [7]. However, the terminology has since been updated to elliptical to more accurately reflect the capability for independent adjustments of the major and minor axes. This also serves to distinguish the elliptical scan strategy from wobbling. Wobbling is commonly employed in laser welding, where the laser path is generated by mechanically or mathematically combining circular and linear motions [8,9]. Scan path-wise, wobbling is a specific case of elliptical scanning in which the major and minor axes of the ellipse are equal; however, wobbling does not involve synchronized adjustments of laser power to the scan path. In contrast, pointwise control in elliptical scanning allows for continuous adjustments to both laser power and speed along the elliptical path, providing full control over the spatiotemporal heat placement.

The second type of temperature field control scan strategy utilizes the Hilbert curve, also known as the Hilbert space-filling curve. This continuous fractal curve efficiently fills a 2D space [10]. The Hilbert curve is advantageous for scan path planning because it offers a mapping between 1D and 2D spaces while effectively preserving locality. In simpler terms, points that are close to each other in the 1D space remain close when mapped to the 2D space, thereby facilitating uniform local heating. Examples of two Hilbert curves are illustrated in Figure 3.

Both the elliptical and Hilbert curve scan paths aim to establish localized heating patterns. These patterns are designed to sustain a local region above the melting point for an extended duration, while also achieving other targeted local thermal conditions. The effectiveness of these temperature field control scan strategies is assessed through a series of experiments, organized into three sets:

1. Linear scan: Single tracks measuring 20 mm in length were scanned. The first group, designated LP01–LP19, was scanned at a speed of 1000 mm/s. The laser power was incrementally increased from 40 W to 400 W in 20 W steps. The second group, LP21 to LP39, was scanned at 500 mm/s but maintained the same power levels as the first group. These linear scans serve as the baseline for comparison.
2. Elliptical scan: Elliptical scan paths of 10 mm in length were executed using the parameters listed in Table 1. The hatching space (h) is set at 0.1 mm, and the scanning speed is 1000 mm/s.

Table 1. Elliptical scan experiment parameters

Part #	EP01	EP02	EP03	EP04	EP05	EP06	EP07	EP08
2a (mm)	1.00	0.50	0.50	0.25	1.00	0.50	0.50	0.25
2b (mm)	1.00	1.00	0.50	0.50	1.00	1.00	0.50	0.50
Power (W)	400				200			

3. Hilbert curve: Two Hilbert curves, designated as HP01 and HP02, were programmed with hatching distances of 0.1 mm and 0.2 mm, respectively. Each was set to run at a nominal speed of 1000 mm/s and a laser power of 200 W. The curves were interpreted using the 'constant power density' and 'exact stop' modes in SAM [11]. Due to frequent directional changes and associated acceleration constraints, the nominal scan speed could not be reached. As a result, laser power was adjusted to maintain a constant power density. Figure 3 color-codes the speed and power for the two Hilbert curve scan strategies after the interpretation.

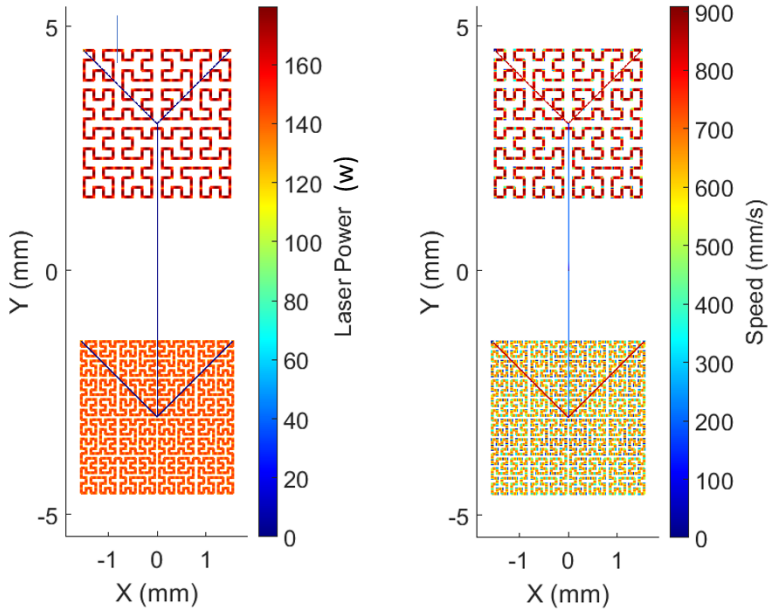

Figure 3. Hilbert Curve Scan Strategies: The lower curve (HP01) features a hatching distance of 0.1 mm, while the upper curve (HP02) exhibits a hatching distance of 0.2 mm.

The Hilbert curve scan strategies provide the most compelling demonstration of the continuous adjustments in laser power and speed made possible by pointwise control. Through these experimental setups, we aim to validate the efficacy of the temperature field control scan strategies in achieving localized heating and, consequently, desired material properties.

Experiments

The experimental setup is shown in Figure 4. It employs a prototype system developed for the NIST AMMT upgrade. The prototype utilizes the same pointwise control technology but incorporates a new galvo that offers substantially higher dynamic response. Experiments were conducted on a nickel superalloy 625 (IN625) bare metal plate that measures approximately 100 mm x 25 mm x 6.5 mm (Length x Width x Thickness) and is situated in an Argon gas environment. A high-speed camera, coaxially aligned with the processing laser, monitored the proceedings. Thermal radiation emanating from the MP and traveling in the direction opposite to the heating laser was redirected toward the monitoring camera via a dichroic mirror. Bandpass filtering was achieved using an 800 nm long-pass filter stacked with a 950 nm short-pass filter. The camera operated with an integration time of 25 µs and a trigger interval of 60 µs. Its image window was configured to 128 pixels x 128 pixels, featuring a 10-bit depth and a pixel resolution of 20 µm.

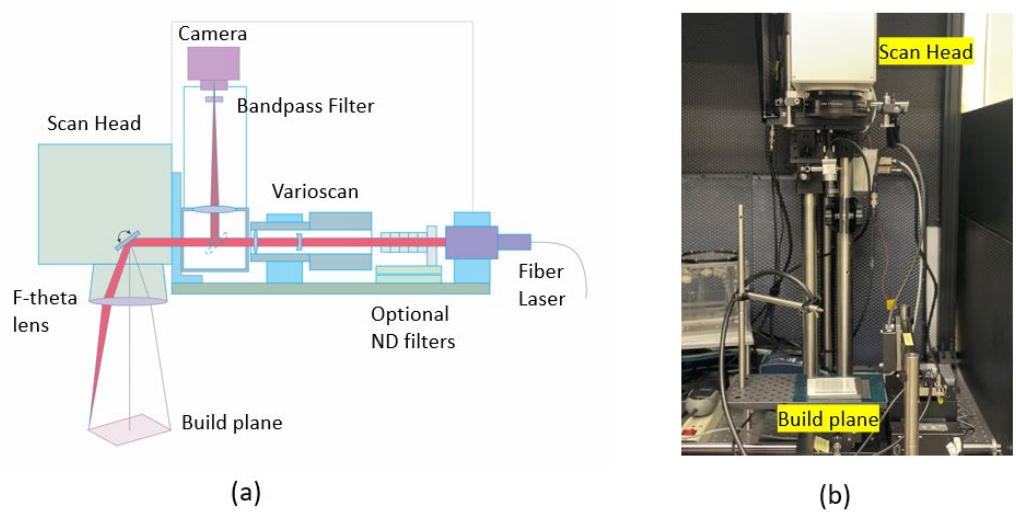

Figure 4. Experimental setup for evaluating temperature field control scan strategies. (a) Schematic shows the laser control and coaxial imaging setup. (b) A picture of the setup.

Laser calibration

It is imperative that the galvo system consistently follows its commanded positions. This necessitates operating the galvo within its maximum acceleration constraints as detailed in [12]. The galvo's acceleration is calibrated by oscillating the laser guide beam with a sinusoidal motion described by $X(t) = A \cdot \sin(2\pi \cdot f \cdot t)$, where A is amplitude, f is frequency, and t is time. The laser position was recorded at 50 000 frames per second (fps) using a high-speed camera set so that the guide beam scanned directly on the camera's pixel array. These positions are plotted in Figure 5

under the label 'Measured Amplitude'. Simultaneously, $X(t)$ is plotted as 'Command Amplitude', and its second derivative is plotted as 'Command Acceleration'.

The right-hand section of the figure provides a closer look at accelerations reaching up to 10^7 mm/s^2. The Measured Amplitude aligns closely with the Command Amplitude for accelerations as high as about 5 x 10^7 mm/s^2. For this study, all scan paths were programmed with an acceleration of 10^7 mm/s^2 to ensure the precise temporal positioning of the laser.

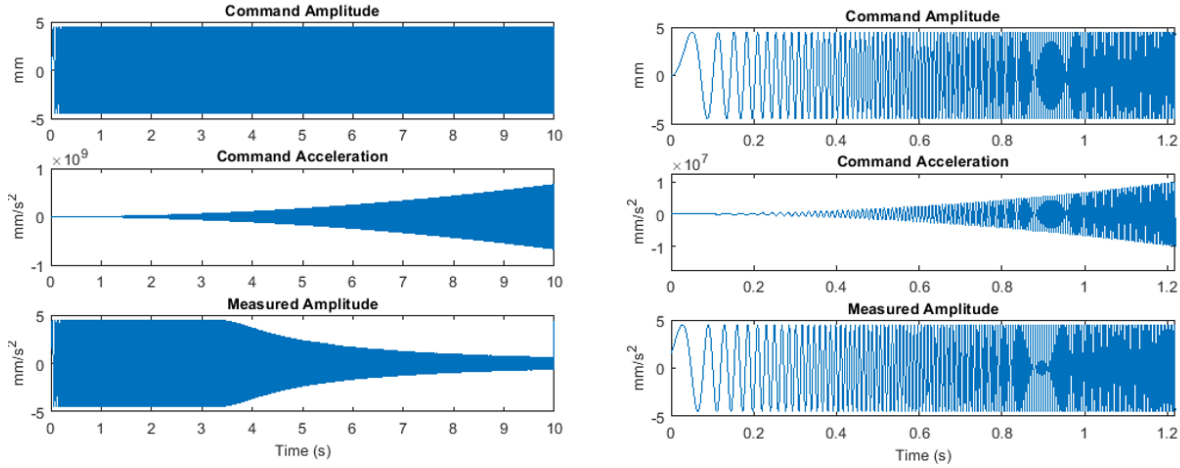

Figure 5. Galvo acceleration calibration results.

In addition to calibrating the galvo's acceleration, it is also essential to calibrate its position, laser power, and laser spot size to ensure optimal performance. For this experiment, the galvo's position is calibrated using an optical target, following a method similar to the one outlined in [13]. The laser spot size is calibrated using a look-up camera as detailed in [14], and is set to 85 µm. For laser power calibration, a laser power meter is placed on the build plane to measure energy absorption. The calibration results are presented in Figure 6, where 'V_{in}' represents the analog voltage input used for setting the laser power, and 'Power' is the corresponding reading from the power meter. It's worth noting that these calibration data take into account potential power loss along the laser's optical path. This can differ significantly from the nominal V_{in}–Laser power relationship typically provided by the laser manufacturer. The calibration curve in Figure 6 is applied for laser power control.

V_{in} (V)	Power (W)
1.157	32.2
2.119	77.6
3.077	123
4.044	170
5.007	216
5.969	262
6.93	307
7.89	352
8.86	397
9.66	432

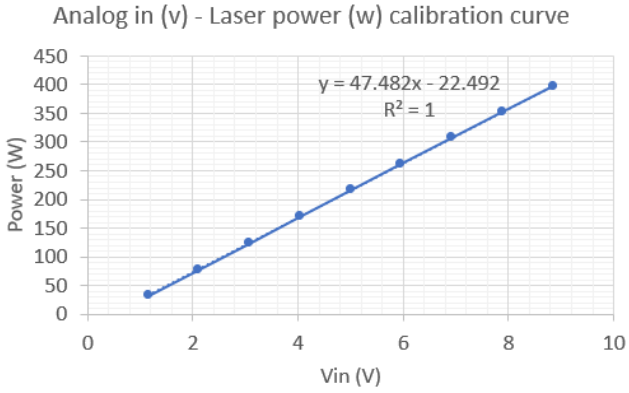

Figure 6. Laser power calibration results.

Camera black-body calibration

The coaxial MP monitoring setup was calibrated directly against a high-temperature blackbody at various temperature settings. A sample image captured at 1200 °C with a 25 µs exposure time is shown in Figure 7a, accompanied by both a contour plot and an x-y profile. Figure 7b presents additional data points along with the Sakuma-Hattori (S-H) curve fitted to these points. The S-H curve is defined as $T = c_2/(A\ln(C/S+1)) - B/A)$ -273), where T is the temperature in °C, c_2 is the second radiation constant (c_2 = 0.014387752 m·K), and S is signal in digital levels (DL). The coefficients A, B, and C of the S-H curve fit are 7.4207 x 10^{-7}, 2.3471 x 10^{-4}, and 6.2160 x 10^{6}, respectively. The coefficient of determination (R^2) for the fit is 0.9985.

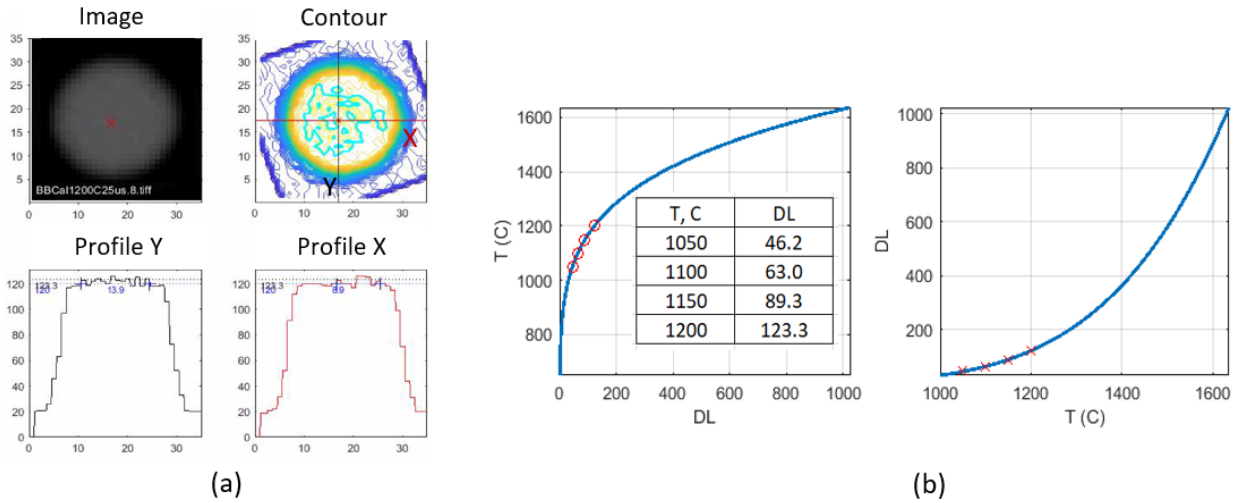

Figure 7. Temperature calibration for the melt MP monitoring camera. (a) The top section displays a sample image of the black body along with its contour plot (axes in units pixels); the bottom section illustrates the temperature profile along the X- and Y-axes (y-axis in DL, x-axis in pixels). (b) Calibration curves are presented, where 'T' represents the set temperature of the black body, and 'DL' indicates the digital level of the black body image.

Temperature history analysis method

To convert the intensity of the MP image into temperature, it is first necessary to determine the emissivity. Emissivity is a measure of an object's ability to emit infrared energy compared to a blackbody at the same temperature. Its values can range from 0 (a shiny mirror) to 1.0 (a blackbody). Accurately measuring emissivity in the AM process can be prohibitively difficult [15], but a close estimation can be made based on the object's melting point temperature. This is achieved using our coaxial image-based temperature history analysis method, as illustrated in Figure 8 and Figure 9.

In these figures, a single track measuring 20 mm in length is scanned from coordinates (-10, 5) mm to (10, 5) mm using a laser with a power setting of 220 W and a speed of 500 mm/s. A rectangular Region of Interest (ROI) with dimensions of 0.1 mm x 0.02 mm is highlighted by

circles in the four sample MP image frames depicted in Figure 8. This ROI is strategically situated at the midpoint of the track to ensure that a steady state has been reached. The four sample frames capture various phases: as the laser approaches, passes through, and then moves away from the ROI. For added clarity, each frame includes annotations: the ROI's coordinates in the build setup are displayed in the top left corner, while the average temperature within the ROI is shown in the top right corner. The global and local frame numbers are provided at the bottom right of each frame.

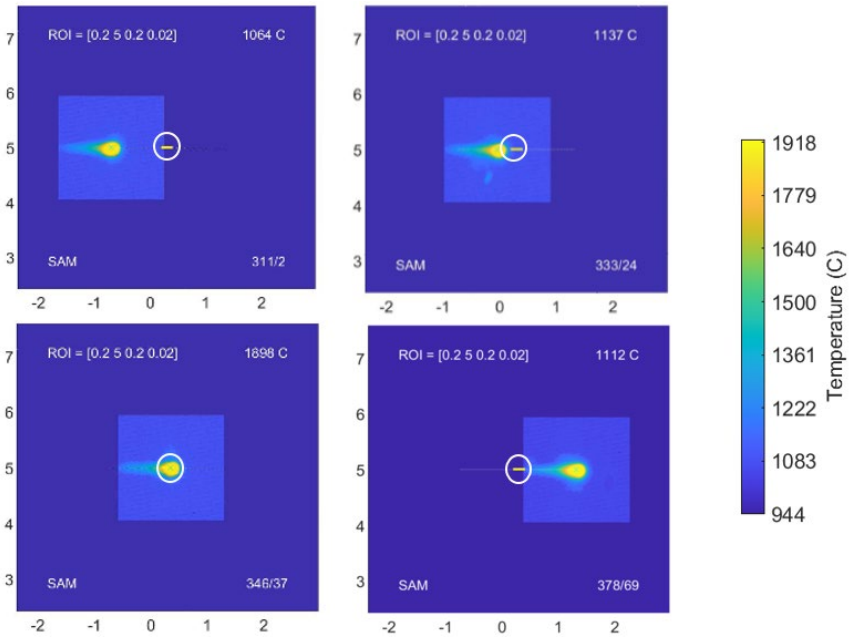

Figure 8. Sample MP image frames for temperature history analysis. Axis units are in mm.

To construct the temperature history for the Region of Interest (ROI), all MP images intersecting with the ROI are identified and annotated with their frame numbers. Given the image resolution of 0.02 mm per pixel, each ROI spans 10 pixels. The digital level (DL) for each pixel within the ROI is recorded for every frame and then converted into temperature using the S-H curve with a trial emissivity (ε) value – let's say ε = 0.4. These temperature data are subsequently plotted against the local frame numbers, as shown in Figure 9a.

Due to a slight delay as the laser passes through each pixel, the temperature profiles exhibit minor shifts to the right. To align these profiles, we use their falling edges, and their average is then plotted against time (derived from frame numbers) in Figure 9b. Figure 9c displays the first and second time derivatives of the smoothed average temperature profile. Inflection points in the temperature curve are identified by changes in the sign of the second derivative [16]. The trial emissivity value of 0.4 yields a temperature of 1322 °C at the inflection point. Theoretically, the inflection point of the time-temperature curve during the solidification process should correspond to the melting point. This aligns well with the literature-reported melting temperature range for IN625, which is between 1290 °C and 1350 °C.

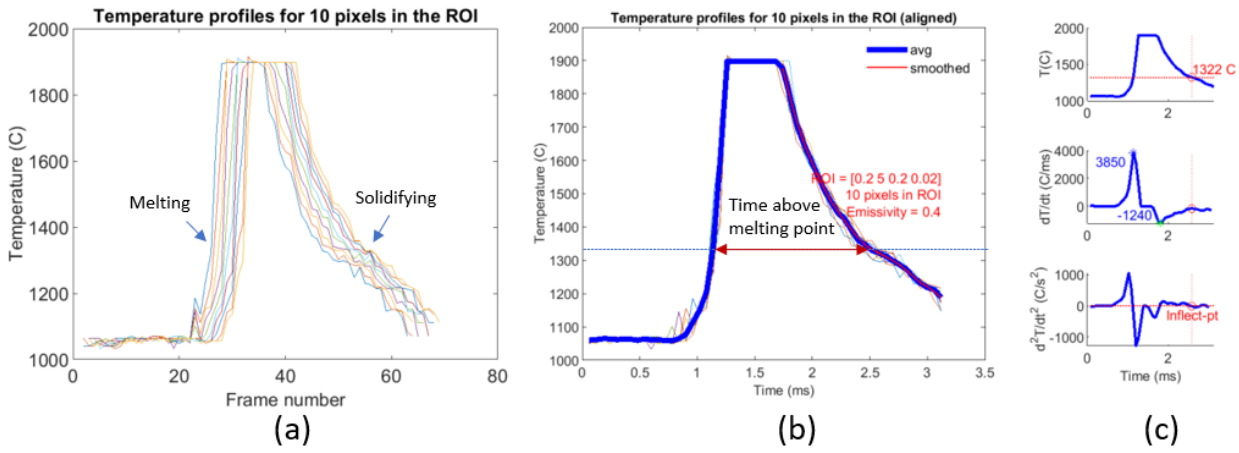

Figure 9. Temperature history analysis for a linear scan at 220 w and 500 mm/s. (a) Temperature profiles for individual pixels. (b) Averaged temperature profile across all pixels. (c) Derivatives of the averaged temperature profile.

Additional analyses of other single-track experiments have yielded melting points that consistently fall within the range of 1300 °C to 1350 °C, assuming an emissivity (ϵ) of 0.4. For example, Figure 10 features an ROI comprising 250 pixels from the central portion of a single track scanned at a power of 220 W and a speed of 1000 mm/s. The solidification point determined in this instance is 1303 °C. To maintain consistency throughout the study, an emissivity of 0.4 is used for all temperature conversions. A reference melting point of 1350 °C, corresponding to a Digital Level (DL) of 116 based on the S-H curve, was selected for analytical purposes. Once the melting point is identified, the duration of time above this temperature can be estimated, as illustrated in Figure 9 and Figure 10. The maximum heating and cooling rates can also be directly derived from the first derivative of the temperature curve; these are 7990 °C/ms and 2300 °C/ms, respectively. These values are averaged over the ROI. The dimensions of the ROI can be adjusted in multiples of the MP image pixel size (i.e., 20 µm x 20 µm). For more complex scan paths, the number of remelts can also be ascertained.

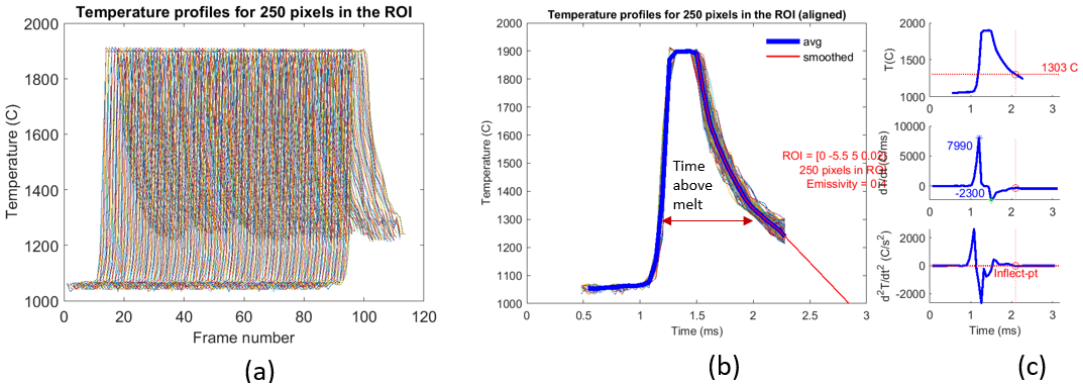

Figure 10. Temperature history analysis for linear scan of 220 W and 1000 mm/s. (a) Temperature profiles for individual pixels. (b) Averaged temperature profile across all pixels. (c) Derivatives of the averaged temperature profile.

This coaxial image-based temperature history analysis method has been utilized to examine the experimental results, and details will be presented in the subsequent sections.

Experiment results and discussion

The scanning process was captured by triggering the coaxial camera at intervals of 60 μs. These images were streamed to a computer in real-time. For linear scans at a speed of 1000 mm/s, 334 frames were captured for each scan, while 667 frames were recorded for each scan conducted at a speed of 500 mm/s. For elliptical scans ranging from EP01 to EP04, the numbers of frames recorded were 4286, 3306, 2265, and 1748, respectively; this pattern was repeated for scans EP05 to EP08. For Hilbert scans, 4945 and 1717 frames were captured for HP01 and HP02, respectively. The MP dimensions from these various scans were first compared. The temperature history analysis method was then employed to investigate the evolution of the MP and the temperature field. A new visualization method, the temperature history map, was also introduced as an efficient means of representing the extensive volume of in-situ monitoring data.

MP dimension

The MP area is estimated by setting a Digital Level (DL) threshold of 116 DL, based on the solidification point identified in the previous section, and then counting the pixels that exceed this threshold. This straightforward method is versatile enough to accommodate complex MP shapes, such as the donut-shaped pools produced by elliptical scans. The dimensions of the MP—namely its length and width—are determined by the lengths of the major and minor axes of the convex hull that encloses the thresholded region. It's worth noting that these dimensions may not align with the instantaneous direction of the laser scan.

Figure 11 presents the MP geometry statistics for the linear scans. Intriguingly, at a speed of 1000 mm/s (for scans LP01-LP19), the MP area displays a convex relationship with laser power, while the length of the MP remains largely unaltered by variations in power. In contrast, at a speed of 500 mm/s (for scans LP21-LP39), the MP area shows a concave relationship with laser power, and both the width and length of the MP increase as the laser power rises.

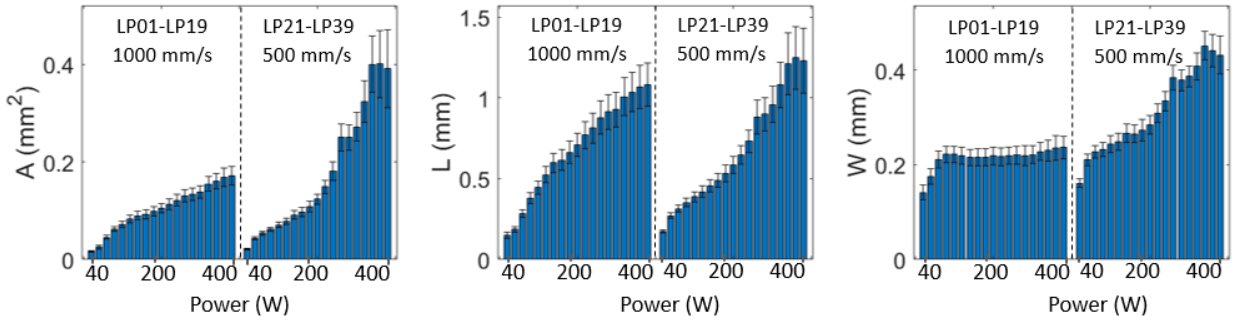

Figure 11. MP statistics for linear scans. A is MP area, L is MP length, W is MP width. Error bars display one standard deviation.

Figure 12 presents the MP geometry statistics for the elliptical scans. For scans at a laser power of 400 W (EP01 – EP04), there is a proportional relationship between the MP length and

the elliptical parameter 'b,' and between the MP width and the elliptical parameter 'a' (as detailed in Table 1). This proportional relationship becomes even more pronounced at a lower laser power of 200 W. For instance, scans EP05 and EP06, which share the same 'b' value, also exhibit identical lengths. Similarly, scans EP06 and EP07, which have the same 'a' value, demonstrate matching widths. These observations underscore the ability to control MP dimensions effectively through the manipulation of elliptical scan parameters.

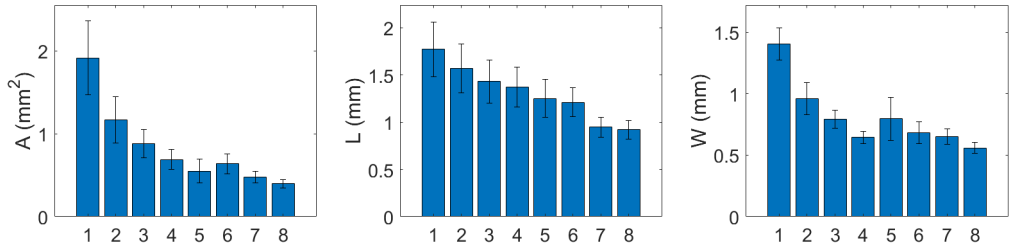

Figure 12. MP statistics for elliptical scans EP01 – EP08, labeled as 1-8. A is MP area, L is MP length, W is MP width. Error bars display one standard deviation.

Figure 13 presents MP statistics for the Hilbert curve scans. Characterized by short scan vectors and frequent directional changes, the power and speed schemes for these scans are detailed in Figure 3. Figure 13b highlights a significant difference in MP aspect ratios between HP01 and HP02. Specifically, the length-to-width ratio of the MP for both is noticeably smaller compared to that of linear scans. This discrepancy is particularly pronounced in HP01, which can be attributed to the use of shorter scan vectors. The frequent changes in scanning direction appear to inhibit the MP from fully extending in length.

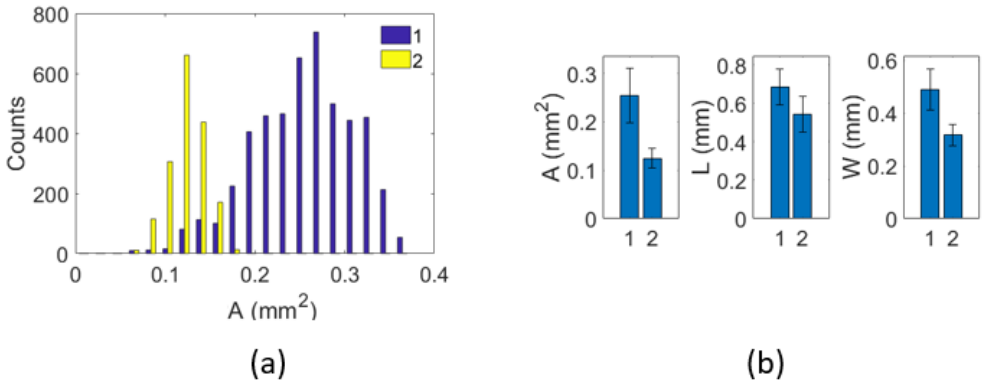

Figure 13. MP statistics for Hilbert curve scans HP01 and HP02, labeled as 1 and 2. A is MP area, L is MP length, W is MP width. Error bars display one standard deviation.

The statistical analysis of MP images highlights distinct differences between elliptical and Hilbert curve scans as opposed to conventional linear scans. In elliptical scans, the MP area is 5 to 10 times larger than that generated by linear scans with similar laser power and speed settings. While the disparity in MP area between Hilbert curve and linear scans is less pronounced, the length-to-width ratio of the MP in Hilbert curve scans is notably smaller. Microscopic examination of the physical tracks further clarifies these differences. Figure 14 shows optical microscope images of select scans. Notably, in elliptical scans the track width does not necessarily align with the MP width. The chevron patterns seen in these scans are also markedly different

from those in linear scans. In the case of Hilbert curve scans, the MP solidifies into a unique pattern. This is influenced not only by the shape of the MP but also by the scan path, which in turn affects the flow of molten metal.

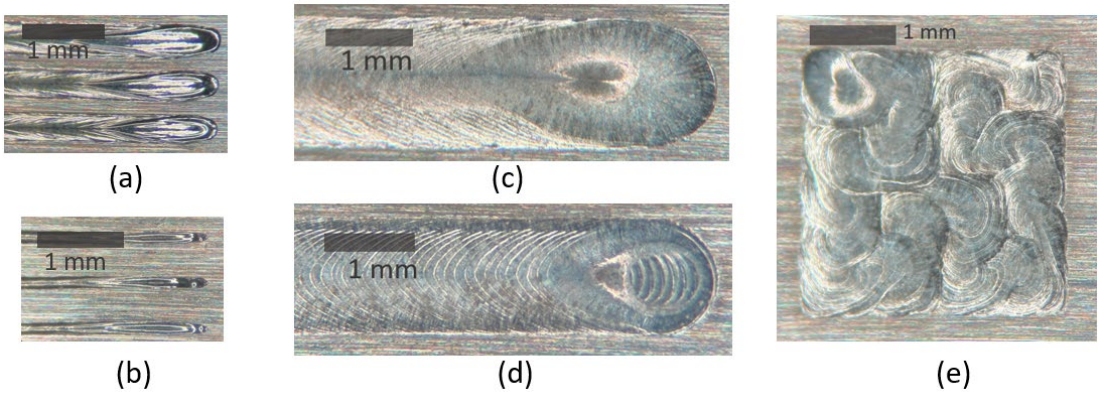

Figure 14. Microscopic examination of selected tracks. (a) Linear scans at a speed of 500 mm/s for LP37, LP38, and LP39 (from bottom to top), with corresponding laser powers of 360 W, 380 W, and 400 W, respectively. (b) Linear scans at a speed of 1000 mm/s for LP17, LP18, and LP19 (from bottom to top), with corresponding laser powers of 360 W, 380 W, and 400 W. (c) EP01: Elliptical scan conducted at a laser power of 400 W. (d) EP05: Elliptical scan executed at a laser power of 200 W. (e) HP01: Hilbert curve scan with a hatching distance of 0.1 mm.

MP evolution in elliptical scans

Figure 15 presents the outcomes from the elliptical scan EP05, as detailed in Table 1. Figure 15a displays four frames captured during the initial phase of the scan. The MP undergoes a transformation, starting from a conventional teardrop shape in the second frame and evolving into an expansive elliptical shape by the fourth frame. Temperature profiles shown in Figure 15b indicate that multiple re-melts occur at the region of interest (ROI). These re-melts contribute to the formation of a doughnut-shaped MP with an unmelted center, as illustrated in the fourth frame of Figure 15a. This characteristic is further corroborated by the microscopic image of EP05 displayed in Figure 14d.

Figure 16 presents the results from elliptical scan EP01, which utilizes the same parameters as EP05 but with an increased laser power of 400W. Figure 16a displays four frames captured during the concluding phase of the scan, with the final frame bearing a resemblance to the image shown in Figure 14c. Temperature profiles depicted in Figure 16b indicate that, when laser power is sufficiently high, the region of interest (ROI) remains above the melting point through multiple cycles without requiring re-melts. Contrary to the doughnut-shaped MP observed in EP05, the MP in EP01 forms a fully filled elliptical shape.

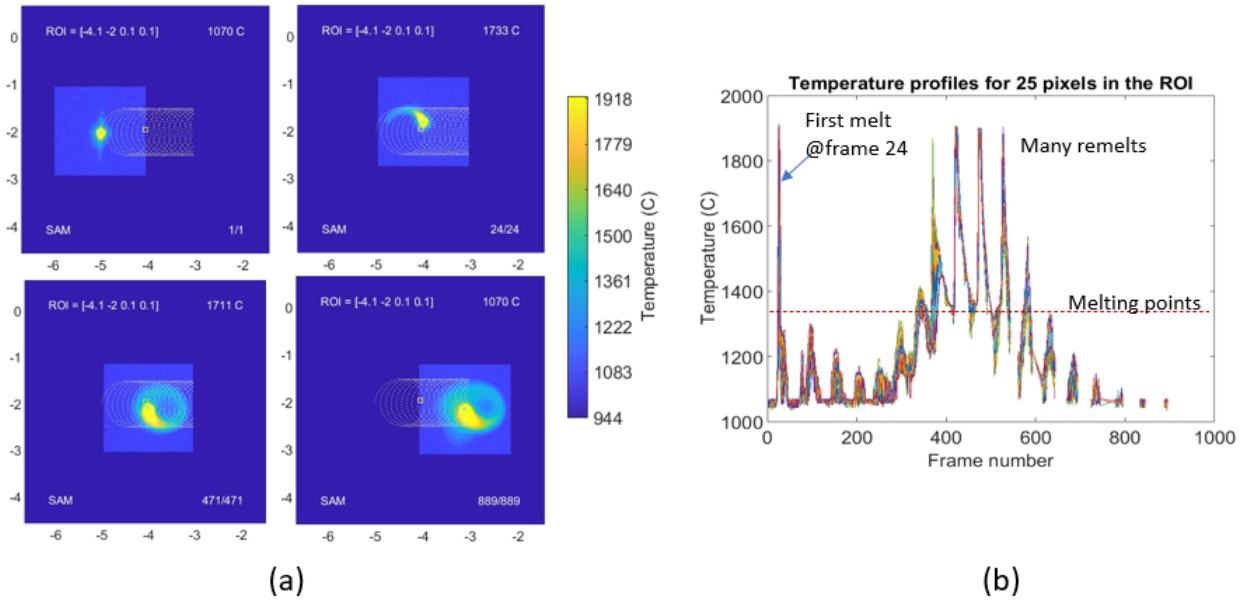

Figure 15. Temperature history analysis for elliptical scan of EP05. (a) Four frames at the beginning of the track. (b) Corresponding temperature history at the ROI.

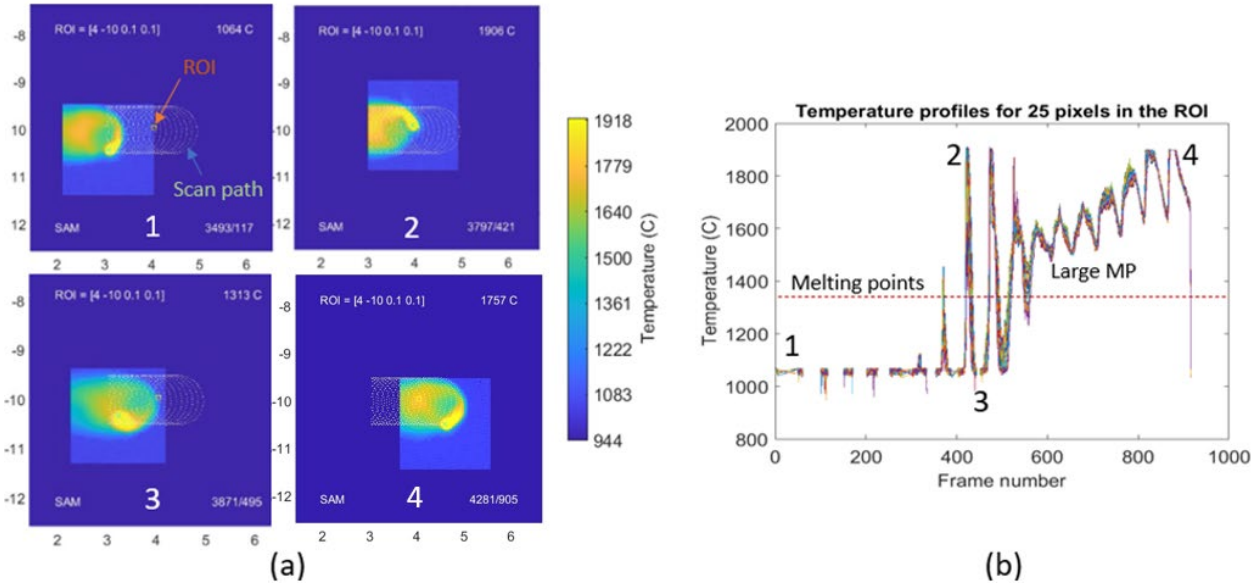

Figure 16. Temperature history analysis for elliptical scan of EP01. (a) Four frames at the end of the track. (b) Corresponding temperature history at the ROI.

The data presented in Figure 12 may initially seem counterintuitive. While both the MP length and width of EP05 appear larger than those of EP06, the MP area for EP06 is actually greater. This apparent contradiction can be resolved by understanding the methodology behind calculating the MP area, length, and width. EP05 has larger dimensions with 2a being 1 mm and 2b being 1 mm (according to Table 1), but it also includes an unmelted region within its doughnut-shaped MP. On the other hand, EP06 has smaller diameters, with 2a at 0.5 mm and 2b at 1 mm, but is completely melted in the center. As a result, the MP area for EP06 is larger due to the absence of an unmelted region.

Temperature history map

Thus far, our analysis has been confined to a single ROI. However, it's possible to map multiple adjacent ROIs together to create temperature history maps, which can be color-coded based on the average pixel value within each ROI. The size of the ROI can be defined as any multiple of the coaxial image pixel size. Figure 17 provides comprehensive temperature history maps for the Hilbert curve scan HP02. These maps were generated using temperature profiles similar to those illustrated in Figure 15b and Figure 16b. In these maps, the following metrics are presented: (a) Maximum Temperature: This captures the highest temperature ever recorded for each ROI (the camera reaches saturation at 2000C with the current settings). (b) Maximum Cooling Rate: This is calculated from the first melting event but can be adjusted to include subsequent remelting events if desired. (c) Total Time Above Melt: This metric indicates the aggregate duration during which the ROI's temperature remained above the melting point. (d) Longest Time Above Melt: This represents the longest continuous span during which the temperature in the ROI remained above the melting point. (e) Number of Remelts: This counts the number of instances where the temperature profile crosses back over the melting point. For context, a microscope image of the scan area corresponding to HP02 is displayed in Figure 17f. By considering these multiple aspects, we gain a multi-dimensional understanding of the thermal history of each ROI, which allows for more nuanced interpretations and potential optimizations in the AM process.

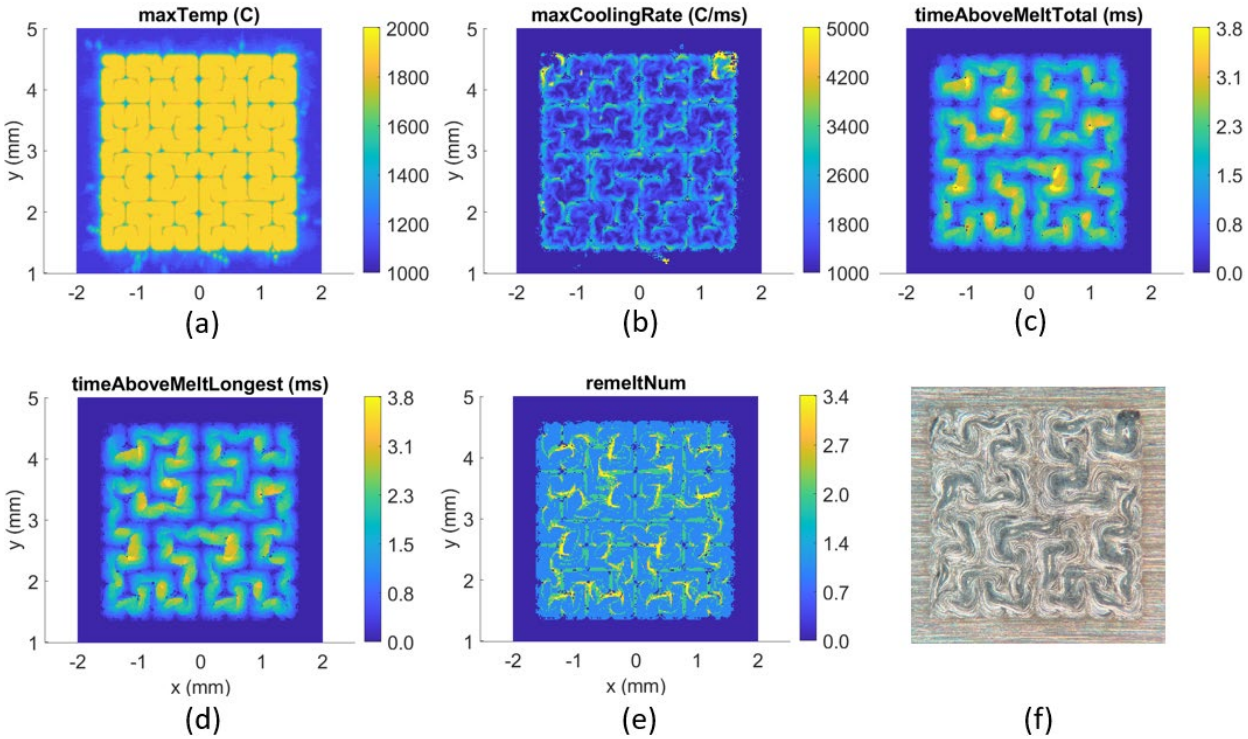

Figure 17. Temperature history maps for Hilbert scan HP02. (a) Maximum temperature. (b) Maximum cooling rate. (c) Total time above melt. (d) Longest time above melt. (e) Number of remelt. (f) Image of the physical tracks.

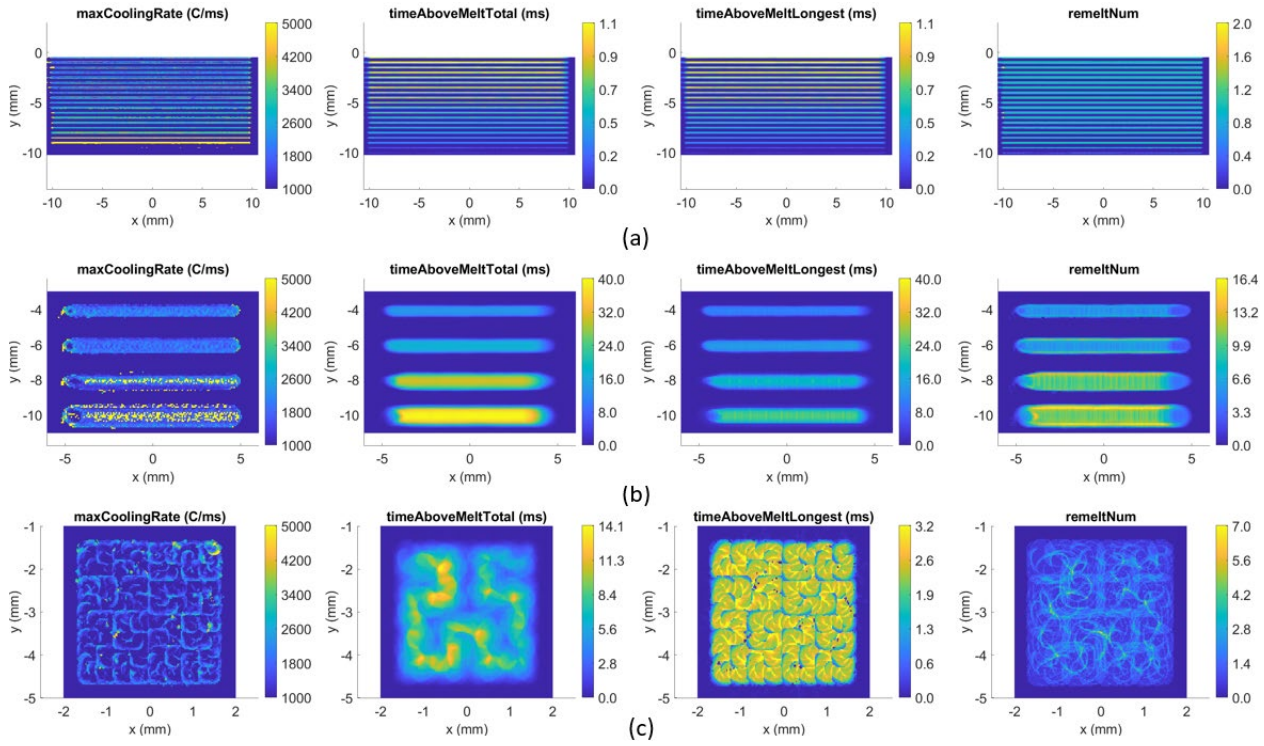

Figure 18. Temperature history maps: (a) Linear Scans LP01 to LP19. (b) Elliptical Scans EP01 to EP04. (c) Hilbert Scan HP01. Note: The range of the scale bars has been adjusted to highlight the variation within the series.

The creation of temperature history maps serves to effectively analyze the extensive MP image data generated by high-speed cameras. These maps not only offer a useful tool for comparing different scanning strategies but also provide invaluable insights for process control optimization and quality prediction of the finished part. Figure 18 presents example temperature history maps for a range of scanning strategies, including linear, elliptical, and Hilbert curve scans. Several key observations can be made based on these maps:

1. Maximum Temperature: The current camera setting is for capturing the lower temperature range around the metal melting point (1000 °C to 2000 °C). The maximum temperature history maps such created are useful for detecting lack of fusion regions (Figure 17). However, due to the rapid saturation of the camera sensor at high temperatures, temperature information higher than 2000 °C is lost. The maximum temperature history maps were not shown in Figure 18 since they are saturated most of time. Future experiments are planned with shorter exposure times to capture nuanced differences in higher temperature regimes across various scanning strategies.
2. Maximum Cooling Rate: The variance in the maximum cooling rate across different scanning strategies is marginal. The unusually high cooling rates (indicated by bright spots on the map) are typically attributed to hot spatters. To enhance this aspect of the analysis, several improvements could be considered: (a) More effective methods for spatter removal. (b) Utilizing a wider dynamic range for temperature measurements. (c) Performing separate cooling rate analyses for the liquid and solid states.

3. Total Time Above Melt (T_t): In the case of linear scans, higher power settings result in a longer T_t. For elliptical scans, T_t increases with larger diameters. Overall, elliptical scans yield a substantially longer T_t compared to linear scans. The Hilbert curve scans create very unique patterns for the T_t map. The long-range pattern of the Hilbert curve path is more obvious in HP01 (Figure 18) than HP02 (Figure 17).
4. Longest Time Above Melt (T_s): For linear scans, T_s and T_t are practically identical. Elliptical scans show a longer T_s for larger diameters, which is the similar trend as what is observed for T_t. Once again, elliptical scans significantly outlast linear scans in terms of T_s. The T_s in Hilbert curve scans resembles more the short-range pattern of their paths. Interesting enough, the microscopic images show the physical tracks follows the T_t pattern more than the T_s pattern.
5. Number of Remelts (N_r): In linear scans, N_r is consistently equal to 1 with occasional exceptions at the beginnings of some lines, likely due to spatters. In elliptical scans, N_r increases with the diameter size. For Hilbert scans, N_r varies greatly; yet a clear trace resembling the scan path can be observed. It is important to note that since N_r is averaged over all the pixels within the ROI, it may not necessarily be an integer.

The temperature history maps provide much information in a nutshell. The information not only deepen the understanding of the thermal characteristics of different scanning strategies but also pave the way for enhancements to both the process and the quality of the final product.

It's worth highlighting that, unlike elliptical scans, Hilbert curve scans visit each location only once. Therefore, the Hilbert curve could also be applicable to Directed Energy Deposition (DED) AM processes. This characteristic also makes them comparable to conventional LPBF raster hatching strategies in terms of the distance needed to cover an area, as well as the average laser power input density. Hilbert scans produce larger MP than linear scans due to the efficient utilization of residual heat, similar to conventional scans that employ short, adjacent scan vectors. However, Hilbert curves harness this residual heat in a more controlled manner, potentially leading to a more uniform and energy-efficient build. Additionally, each Hilbert cell can be considered a voxel. Different laser power and speed settings can be applied to each voxel, potentially enabling fine-grained control over material properties. This level of control over the local temperature field represents a significant advancement toward voxel-level control in AM.

Both elliptical and Hilbert curve scans leverage local residual heat and reheating, creating a much larger heat-affected zone and distinctive local temperature field patterns compared to conventional raster scans. Despite these similarities, Hilbert curve functions more as a non-cross-over infill strategy, and remelting events are less frequent and occur solely due to neighborhood effects. Prior work has demonstrated that reheating scan strategies can promote the formation of martensite in stainless steel 17-4 parts [17,18]. This suggests that functionally graded materials could be constructed through improved control of the temperature field, a notion supported by our own studies [7]. A recent study by Wu et al. [19] provided the first observations of wobbling scans under synchrotron X-ray and noted a reduction in keyhole formation. This phenomenon was attributed by the authors to a decrease in energy density. Our in-situ MP monitoring indicates that elliptical scans can actually create much larger MP, which could potentially mitigate keyhole pore formation in traditionally vulnerable regions. Additionally, Huang et al. demonstrated that surface roughness can be improved through a wobble scan strategy [9]. These findings suggest

the potential for better control of material properties, improved surface finishes, and more effective AM processes through temperature field control, thereby paving the way for a new paradigm in Laser Powder Bed Fusion.

Summary

In this study, we introduce the concept of temperature field control as a significant advancement toward voxel-level control in AM. We have developed a methodology for analyzing temperature histories from coaxial MP images and have created temperature history maps to facilitate the direct comparison of various scanning strategies. Our work demonstrates the temperature field changes by scanning strategies building upon pointwise AM control technology. Specifically, we highlight the versatility of elliptical scanning in generating a wide range of temperature histories, as well as the utility of the Hilbert curve scanning strategy for achieving uniform local heating. We also discuss the potential these strategies offer for voxel-level material property control and energy-efficient builds, with further research planned in these areas. Elliptical and Hilbert curve scans represent two distinct approaches to temperature field control, each with its own unique benefits and limitations. We anticipate that such control strategies will eventually become standard hatching patterns in AM.

Reference

[1] King WE, Anderson AT, Ferencz RM, Hodge NE, Kamath C, Khairallah SA, et al. Laser powder bed fusion additive manufacturing of metals; physics, computational, and materials challenges. Applied Physics Reviews 2015;2:041304.

[2] Bhavar V, Kattire P, Patil V, Khot S, Gujar K, Singh R. A review on powder bed fusion technology of metal additive manufacturing, 2014.

[3] Gordon JV, Narra SP, Cunningham RW, Liu H, Chen H, Suter RM, et al. Defect structure process maps for laser powder bed fusion additive manufacturing. Additive Manufacturing 2020;36:101552. https://doi.org/10.1016/j.addma.2020.101552.

[4] Malekipour E, El-Mounayri H. Common defects and contributing parameters in powder bed fusion AM process and their classification for online monitoring and control: a review. Int J Adv Manuf Technol 2018;95:527–50. https://doi.org/10.1007/s00170-017-1172-6.

[5] Lane et al. Design, Developments, and Results from the NIST Additive Manufacturing Metrology Testbed (AMMT). Solid Freeform Fabrication 2016: Proceedings of the 26th Annual International Solid Freeform Fabrication Symposium n.d.

[6] Yeung H, Hutchinson, Keely J, Lin, Dong B. Design and Implementation of Laser Powder Bed Fusion Additive Manufacturing Testbed Control Software. Solid Freeform Fabrication 2021: Proceedings of the 32th Annual International Solid Freeform Fabrication Symposium n.d.

[7] Yeung H, Chen J, Yang G, Guo Y, Lin D, Tan W, et al. Effect of spiral scan strategy on microstructure for additively manufactured stainless steel 17–4. Manufacturing Letters 2021;29:1–4. https://doi.org/10.1016/j.mfglet.2021.04.005.

[8] Matthias S, Lucas M, Sivam S, Bhut B. Using wobble based laser scanning techniques in additive manufacturing applications. Lasers in Manufacturing Conference 2019 n.d.

[9] Huang T-Y, Cheng C-W, Lee A-C, Chang T-W, Tsai M-C. Influence of Wobble-Based Scanning Strategy on Surface Morphology of Laser Powder Bed-Fabricated Permalloy. Materials 2023;16:2062. https://doi.org/10.3390/ma16052062.
[10] Moon B, Jagadish HV, Faloutsos C, Saltz JH. Analysis of the clustering properties of the Hilbert space-filling curve. IEEE Trans Knowl Data Eng 2001;13:124–41. https://doi.org/10.1109/69.908985.
[11] Yeung H, Neira J, Lane B, Fox J, Lopez F. Laser Path Planning and Power Control Strategies for Powder Bed Fusion Systems. Solid Freeform Fabrication 2016: Proceedings of the 27th Annual International Solid Freeform Fabrication Symposium n.d.
[12] Yeung H, Lane BM, Donmez MA, Fox JC, Neira J. Implementation of Advanced Laser Control Strategies for Powder Bed Fusion Systems. Procedia Manufacturing 2018;26:871–9. https://doi.org/10.1016/j.promfg.2018.07.112.
[13] Yeung H, Lane BM, Donmez MA, Moylan S. In-situ calibration of laser/galvo scanning system using dimensional reference artefacts. CIRP Annals 2020:S0007850620300160. https://doi.org/10.1016/j.cirp.2020.03.016.
[14] Yeung H, Grantham S. Laser Calibration for Powder Bed Fusion Additive Manufacturing Process. Solid Freeform Fabrication Symposium 2022, Austin, TX, US n.d.
[15] Deisenroth DC, Mekhontsev S, Lane B, Hanssen L, Zhirnov I, Khromchenko V, et al. Measurement Uncertainty of Surface Temperature Distributions for Laser Powder Bed Fusion Processes. J RES NATL INST STAN 2021;126:126013. https://doi.org/10.6028/jres.126.013.
[16] Heigel JC, Lane BM. Measurement of the Melt Pool Length During Single Scan Tracks in a Commercial Laser Powder Bed Fusion Process. Journal of Manufacturing Science and Engineering 2018;140:051012. https://doi.org/10.1115/1.4037571.
[17] Rafi HK, Pal D, Patil N, Starr TL, Stucker BE. Microstructure and Mechanical Behavior of 17-4 Precipitation Hardenable Steel Processed by Selective Laser Melting. J of Materi Eng and Perform 2014;23:4421–8. https://doi.org/10.1007/s11665-014-1226-y.
[18] Rashid R, Masood SH, Ruan D, Palanisamy S, Rahman Rashid RA, Brandt M. Effect of scan strategy on density and metallurgical properties of 17-4PH parts printed by Selective Laser Melting (SLM). Journal of Materials Processing Technology 2017;249:502–11. https://doi.org/10.1016/j.jmatprotec.2017.06.023.
[19] Wu Z, Tang G, Clark SJ, Meshkov A, Roychowdhury S, Gould B, et al. High frequency beam oscillation keyhole dynamics in laser melting revealed by in-situ x-ray imaging. Commun Mater 2023;4:5. https://doi.org/10.1038/s43246-023-00332-z.